Exp Fluids (2012) 53:319–330
DOI 10.1007/s00348-012-1290-8

RESEARCH ARTICLE

Assessment of the derivative-moment transformation method for unsteady-load estimation

Ali Mohebbian · David E. Rival

Received: 17 August 2011 / Revised: 1 March 2012 / Accepted: 4 March 2012 / Published online: 20 March 2012

Abstract It is often difficult, if not impossible, to measure the aerodynamic or hydrodynamic forces on a moving body. For this reason, a classical control-volume technique is typically applied to extract the unsteady forces. However, measuring the acceleration term within the volume of interest using particle image velocimetry (PIV) can be limited by optical access, reflections, as well as shadows. Therefore, in this study, an alternative approach, termed the derivative-moment transformation (DMT) method, is introduced and tested on a synthetic data set produced using numerical simulations. The test case involves the unsteady loading of a flat plate in a two-dimensional, laminar periodic gust. The results suggest that the DMT method can accurately predict the acceleration term so long as appropriate spatial and temporal resolutions are maintained. The major deficiency, which is more dominant for the direction of drag, was found to be the determination of pressure and unsteady terms in the wake. The effect of control-volume size was investigated, suggesting that larger domains work best by minimizing the associated error in the determination of the pressure field. When decreasing the control-volume size, wake vortices, which produce high gradients across the control surfaces, are found to substantially increase the level of error. On the other hand, it was shown that for large control volumes, and with realistic spatial resolution, the accuracy of the DMT method would also suffer. Therefore, a delicate compromise is required when selecting control-volume size in future experiments.

A. Mohebbian · D. E. Rival (✉)
Department of Mechanical and Manufacturing Engineering, University of Calgary, Calgary, AB, Canada
e-mail: derival@ucalgary.ca

1 Introduction

As described in Rival et al. (2009), it is often not possible to directly measure the aerodynamic forces on a moving body due to challenges in separating out the inertial contribution. The level of unsteadiness of the system is often described through the reduced frequency

$$k = \frac{\pi f c}{U_\infty}, \tag{1}$$

where f is the frequency of motion, c is the appropriate length scale of the body, and U_∞ is the free-stream velocity. It was shown that as one increases the reduced frequency, the measurement error grows inversely proportional to the square of reduced frequency since

$$k^2 \propto \left(\frac{f}{U_\infty}\right)^2, \tag{2}$$

where the aerodynamic and inertial forces are themselves proportional to U_∞^2 and f^2, respectively. On the other hand, at low Reynolds numbers, the integration around the model through direct pressure measurements fails due to low signal-to-noise ratios.

Therefore, the time-resolved aerodynamic force will typically be estimated via particle image velocimetry (PIV) measurements combined with a classic control-volume (momentum balance) approach; see, for example, Rival et al. (2010, 2011). Evaluation of the acceleration term as part of the overall aerodynamic loading requires complete time-resolved velocity measurements within the control volume. However, more often than not, the moving object (e.g., flapping wing) blocks complete optical access via shadows and parallax effects. Furthermore, the laser often produces strong reflections near the object surface where

accelerations are often highest, thus leading to large errors in the prediction of the acceleration term.

Since the early applications of phase-averaged and time-resolved PIV, there have been a number of studies examining force estimation using a classic control-volume approach. In all these examples, measures were taken to access the full velocity field around the model using transparent models, complex optical techniques, etc. These studies include the analysis of steady forces by van Oudheusden et al. (2007) where the control-volume method was applied to a static airfoil at incompressible and compressible conditions. The corresponding pressure field was determined by integrating the differential form of the two-dimensional Navier–Stokes equations. In Unal et al. (1997), the force estimation of an oscillating cylinder in an incompressible inviscid flow was examined. In this case, the control volume was fixed to the oscillating cylinder. In Noca et al. (1997, 1999), a new term containing only vorticity and velocity information was derived so as to replace the pressure term in the Navier–Stokes equations such that the resulting terms were then only dependent on the velocity field and its temporal and spatial derivatives. This procedure also applies to time-varying control volumes, but is generally limited to incompressible flows. Kurtulus et al. (2006) performed time-resolved PIV measurements in order to calculate the unsteady loadings on a square-section cylinder at a Reynolds number of 4,890. Jardin et al. (2009) compared the unsteady-force estimation acting on a hovering foil at low Reynolds numbers using both control-volume and vortex-parameterization methods. Finally, David et al. (2009) applied the classic control-volume method to both experimental and synthetic flow fields so as to identify the effect of various parameters such as spatial and temporal resolutions, as well as the out-of-plane velocity component on the determination of forces.

To avoid the challenge of measuring the velocity field within the control volume—in particular near the model—Wu et al. (2005) applied a transformation of the volume integral into a surface integral. This transformation is termed a derivative-moment transformation (DMT) and was found to produce reliable results on a synthetic two-dimensional data set. It should be noted that this method is only valid for incompressible flows. DMT methods rely on a transformation such as the Gauss' theorem or Föppl transformation so as to convert the volume integral into a surface integral. In this study, the general form of this theorem is defined as follows:

$$\iiint_V \frac{\partial}{\partial x_l} T_{ijk} \mathrm{d}V = \iint_S T_{ijk} n_l \mathrm{d}S, \tag{3}$$

where T_{ijk} can be a scalar, vector or a tensor parameter and n_l is a unit normal vector.

The DMT method is thus advantageous in that only velocity measurements on the control surfaces are required for the overall estimation of loadings. In the current study, we apply this method to our own synthetic data set of a two-dimensional gust on a flat plate. The objective of this study is to determine whether such a method is suitable for unsteady, separated flows and determine what appropriate spatial and temporal resolutions would be necessary when applying PIV to such problems in future experiments.

2 DMT formulation

This section briefly summarizes the DMT methodology used in this study. The unsteady forces on an arbitrary body in an incompressible flow can be obtained from the following integral form of the Navier–Stokes equations:

$$\mathbf{F}(t) = -\rho \iiint_V \frac{\partial \mathbf{u}}{\partial t} \mathrm{d}V - \rho \iint_S \mathbf{u}(\mathbf{u}\cdot\mathbf{n})\mathrm{d}S - \iint_S p\mathbf{n}\mathrm{d}S + \iint_S (\bar{\bar{\tau}}\cdot\mathbf{n})\mathrm{d}S, \tag{4}$$

where $\mathbf{n}$ is the normal vector to the control surface S bounding control volume V, and ρ, $\mathbf{u}$, p and $\bar{\bar{\tau}}$ represent density, velocity, pressure and viscous stress in the fluid, respectively. For a fixed control volume, the Leibniz integral theorem can be applied to the unsteady term in Eq. (4):

$$-\rho \iiint_V \frac{\partial \mathbf{u}}{\partial t} \mathrm{d}V = -\rho \frac{\partial}{\partial t} \iiint_V \mathbf{u}\mathrm{d}V, \tag{5}$$

such that one can reformulate Eq. (4) in the following manner:

$$\mathbf{F}(t) = -\rho \frac{\partial}{\partial t} \iiint_V \mathbf{u}\mathrm{d}V - \rho \iint_S \mathbf{u}(\mathbf{u}\cdot\mathbf{n})\mathrm{d}S - \iint_S p\mathbf{n}\mathrm{d}S + \iint_S (\bar{\bar{\tau}}\cdot\mathbf{n})\mathrm{d}S. \tag{6}$$

It is often the case that some information within the control volume is not accessible with PIV due to reflections, shadows or parallax effects. For this reason, it is useful to transform the volume integral term in Eq. (6) into a surface integral. To achieve this transformation, one may expand the first term on the right-hand side of Eq. (6) in the following manner:

$$\iiint_V u_i \mathrm{d}V = \iiint_V \frac{\partial x_i}{\partial x_j} u_j \mathrm{d}V. \tag{7}$$

Equation (7) is only valid for an orthogonal coordinate system. Therefore, by expanding the right-hand side of this equation, the $i \neq j$ terms are set to zero. Equation (7) can also be rewritten as follows:

$$\iiint_V u_i \mathrm{d}V = \iiint_V \frac{\partial}{\partial x_j}(x_i u_j)\mathrm{d}V - \iiint_V x_i \frac{\partial u_j}{\partial x_j}\mathrm{d}V, \tag{8}$$

where the last term in Eq. (8) vanishes for an incompressible fluid such that:

$$\iiint_V u_i \mathrm{d}V = \iiint_V \frac{\partial}{\partial x_j}(x_i u_j)\mathrm{d}V. \tag{9}$$

The right-hand side of Eq. (9) can be expressed as a surface integral through Gauss' theorem where:

$$\iiint_V \frac{\partial}{\partial x_j}(x_i u_j)\mathrm{d}V = \iint_S x_i u_j n_j \mathrm{d}S. \tag{10}$$

Finally, the volume integral of velocity can be written as follows:

$$\iiint_V u_i \mathrm{d}V = \iint_S x_i u_j n_j \mathrm{d}S. \tag{11}$$

Alternatively, in vector notation, this transformation becomes:

$$\iiint_V \mathbf{u}\mathrm{d}V = \iint_S \mathbf{x}(\mathbf{u}\cdot\mathbf{n})\mathrm{d}S. \tag{12}$$

By substituting Eq. (12) back into the original momentum balance, one obtains a description of the time-resolved forces on an arbitrary body based solely on control-surface information. This reformulation entirely avoids the limitations associated with the measurement of the velocity field near the body itself where accelerations are usually highest:

$$\begin{aligned}\mathbf{F}(t) = &-\rho\frac{\partial}{\partial t}\iint_S \mathbf{x}(\mathbf{u}\cdot\mathbf{n})\mathrm{d}S - \rho\iint_S \mathbf{u}(\mathbf{u}\cdot\mathbf{n})\mathrm{d}S \\ &- \iint_S p\mathbf{n}\mathrm{d}S + \iint_S (\bar{\bar{\tau}}\cdot\mathbf{n})\mathrm{d}S,\end{aligned} \tag{13}$$

where $\mathbf{x}$ is the position vector measured from any fixed frame of reference.

The first and second terms on the right-hand side of Eq. (13) can be obtained by using the measured velocity field, and the last term can be evaluated through the aid of spatial derivatives of the velocity field taken at each point. The third term, which is the pressure distribution along each control surface, is computed by integration of the Navier–Stokes equations from each corner of the CV. Unal et al. (1997), Jardin et al. (2009) and Rival et al. (2010) used this method for the evaluation of pressure:

$$\iint_S \bigtriangledown p \mathrm{d}S = \iint_S \left[\mu \bigtriangleup u - \rho\left(\frac{\partial u}{\partial t} + u\cdot\bigtriangledown u\right)\right]\mathrm{d}S. \tag{14}$$

Equation (15) can now be used, depending on control-surface orientation, to obtain the pressure along the control volume in question:

$$p_n = p_{n-1} + \frac{\partial p}{\partial x}\mathrm{d}x, \qquad p_n = p_{n-1} + \frac{\partial p}{\partial y}\mathrm{d}y. \tag{15}$$

where p_n and p_{n-1} are the values of pressure on the nth and $(n-1)$th nodes. The pressure gradients can be calculated through Eq. (14). In order to obtain the force due to pressure, only relative variations in the pressure distribution from opposing control surfaces are required. Therefore, an arbitrary boundary condition at one corner of the control volume can be used as a starting point, in turn canceling out once the integration is complete. It should be noted that in other studies such as in Kat et al. (2008), the Poisson equation has been used in order to find the pressure distribution instead. This method can also be applied to a thick contour around the body of interest to reduce error propagation, but will not be considered in the current study.

3 Methods

As a starting point for the assessment of the DMT method, numerical simulations are used to produce a synthetic PIV velocity field with realistic vector spacing typical of modern high-speed PIV systems. For this purpose, the unsteady flow over a flat plate (20 mm × 1 mm) is modeled in this study. The plate is exposed to a laminar, periodic gust, which has a time-varying vertical component of velocity. In addition, a uniform free-stream velocity is maintained in the x-direction. For this study, the time step is equal to 0.01 s, and a uniform spatial resolution, equal to 0.001 m, was applied in both directions. The structured, quadrilateral mesh used for the generation of synthetic data included 161,604 nodes and 80,180 elements. The mesh and domain independency of the results for both varying temporal and spatial resolutions was checked in order to ensure that the physics of the problem were properly captured. Moreover, a second-order central finite difference numerical scheme was used for computing temporal and spatial derivatives, and the trapezoidal method was applied for computing spatial integrations. Figure 1 shows a schematic of the numerical domain where the position of various control volumes (CVs) and the flat plate are both defined. The thickness of the plate is $0.05c$, which is

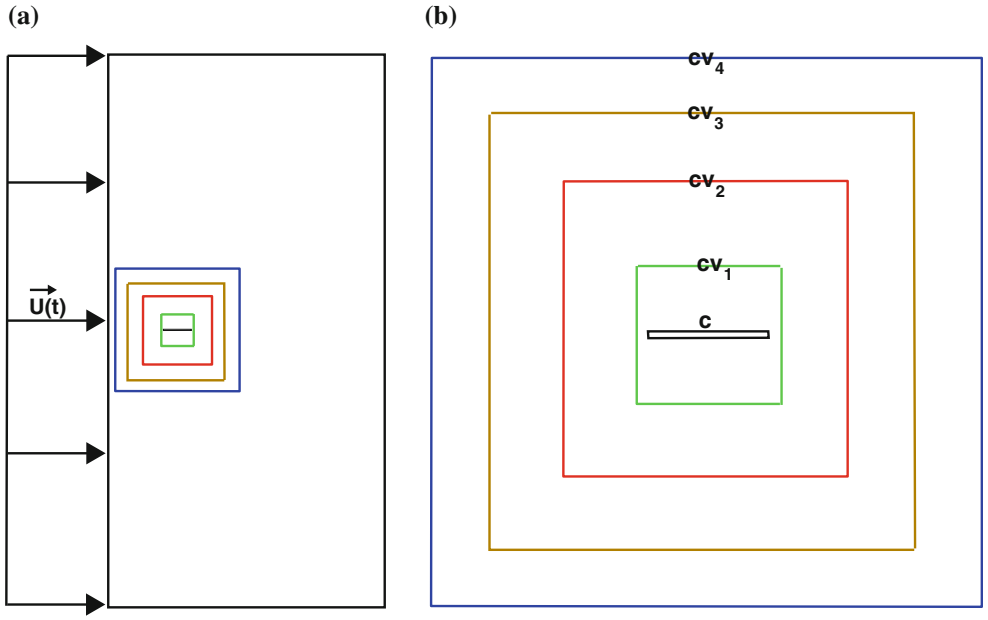

Fig. 1 Positions of various control volumes in the computational domain around the flat plate with chord length c. Note the laminar, periodic boundary condition (*left*). **a** Computational domain ($20c \times 10c$). **b** Close-up of the various control volumes

small enough to be assumed as a thin flat plate. The width and height of the computational domain are equal to $10c$ and $20c$, respectively. One edge of the domain has been considered as an inlet boundary condition, while the rest of the edges are assumed as open boundary conditions. The lengths and widths of CV_1 through CV_4 in Fig. 1 are equal to $1.2c$, $2.5c$, $3.5c$ and $4.5c$, respectively.

For this study, the equations for velocity in the x- and y-directions are as follows:

$$U_x = \text{const.} \qquad U_y = A\sin(2\pi ft), \tag{16}$$

where A is the velocity amplitude in the y-direction, f the gust frequency, and t represents time. The Reynolds number, based on the freestream velocity and chord length (c), was kept at 1,600, which allows for the assumption of laminar flow.

The governing equations were solved using the ANSYS CFX 13.1 commercial package, thus generating a synthetic velocity field within the computational domain. Simulating PIV-like measurements, the velocity field was then used to compute the unsteady aerodynamic loadings, both with classical and DMT methods. The results of these two methods are then compared with the combined pressure and wall shear stress integrations along the flat plate, which in this study will be termed the *direct method*.

During the gust interaction, two vortices of varying strength are produced over the flat plate. In order to gain an appreciation of the flow behavior in this study, Fig. 2 illustrates the vorticity contours at two time steps during the gust period. In this figure, the formation of the leading-

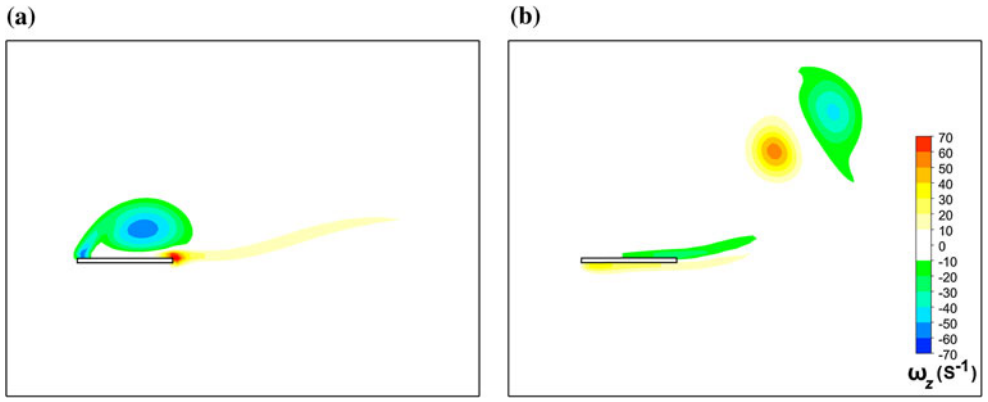

Fig. 2 Vorticity contours at two time steps during the gust period. The *left-hand side* of the figure shows the contour at $t/T = 0.5$ while the *right-hand side* illustrates the vortical wake at $t/T = 0.75$. **a** $t/T = 0.5$. **b** $t/T = 0.75$

edge vortex at $t/T = 0.5$, as well as the wake vortices at $t/T = 0.75$, can be observed.

4 Results

4.1 Evaluation of the acceleration term

Figure 3 illustrates a comparison between the classic control-volume approach and the DMT method for the calculation of the unsteady term in the lift and drag directions. It should be noted that in this section, spatial resolution for various CVs is kept constant so that the spacing between velocity vectors is always the same. The number of nodes on each edge of CV_1 through CV_4 is equal to 25, 51, 71 and 91, respectively. The results demonstrate that these two methods are in good agreement with each other for all CVs and in both directions. Note that for all cases, the initial condition at $t/T = 0$ is $U_x = \text{const}$ and $U_y = 0$. The maximum deviation between the classical and DMT methods for CV_1 through CV_4 is less than 5 % for lift and within 5–10 % for drag. These results support the fact that the DMT method is an appropriate tool for calculating the acceleration term in such separated flows. Furthermore, Fig. 3a shows the time when the gust reaches the various control volumes as well as the time when the wake leaves the control volumes. It should be mentioned that the large control volumes contain more unsteadiness due to the inflow of the vertical gust (vertical acceleration). Similarly, for the large control volumes, it can be observed that the unsteadiness remains for a longer time.

4.2 Contributions of unsteady, convective, pressure and viscous terms

Section 4.1 showed that the DMT method is effective in the estimation of the unsteady term. The maximum deviation between the classical and DMT methods was found to be less than 10 %. In this section, the relative contributions of all terms in Eq. (13) will be examined. Figure 4a–d shows a comparison among different terms of Eq. (13) for CV_1 through CV_4 in the direction of lift. In Fig. 4a, the contribution of unsteady, convective, pressure and viscous terms have been investigated for CV_1. It can be seen that for this CV, the convective and pressure terms are significant during a certain period of the cycle and that the unsteady term is important when t/T is in the range of $0.55 \leq t/T \leq 0.65$. Figure 4b–d, which relates to CV_2–CV_4, illustrates that the importance of the pressure term diminishes with increasing CV size. The convective and unsteady terms, however, increase when the pressure term reduces in magnitude. Therefore, according to Fig. 4, increasing the size of the control volumes leads to a decrease in the pressure term and an increase in the convective and unsteady terms. Note that the unsteady term reaches its maximum value when the wake vortices pass across the rear control surfaces. Also of interest is the out-of-phase relationship between the convective and unsteady terms on the overall lift force. Finally, as also observed in Jardin et al. (2009) and David et al. (2009), the viscous term has a nearly negligible contribution for all control volumes considered in this study.

Figure 5 provides a more precise comparison of the viscous and the pressure contributions over the gust cycle. As discussed above, the pressure term diminishes in magnitude with increasing control-volume size. However, the changes in the pressure term is small for CV_2 through CV_4. Figure 5b depicts the distribution of the viscous term. It can be seen that the maximum value of this term is on the order of 10^{-3}, which is less than a 0.25 % contribution to the total value of lift. It should also be noted that the jumps at the beginning of the period are due to the incoming vertical gust at each respective front control surface.

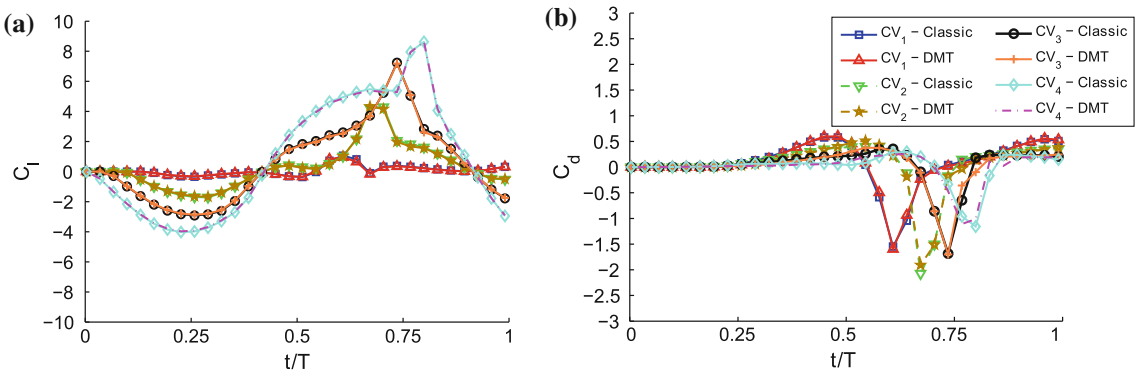

Fig. 3 Comparison between the unsteady term computed by the classic control-volume approach and the unsteady term computed by the DMT method for various CVs with different spatial resolutions and with constant vector spacing; note that the curves have been plotted at every tenth time step for sake of clarity. **a** Lift. **b** Drag

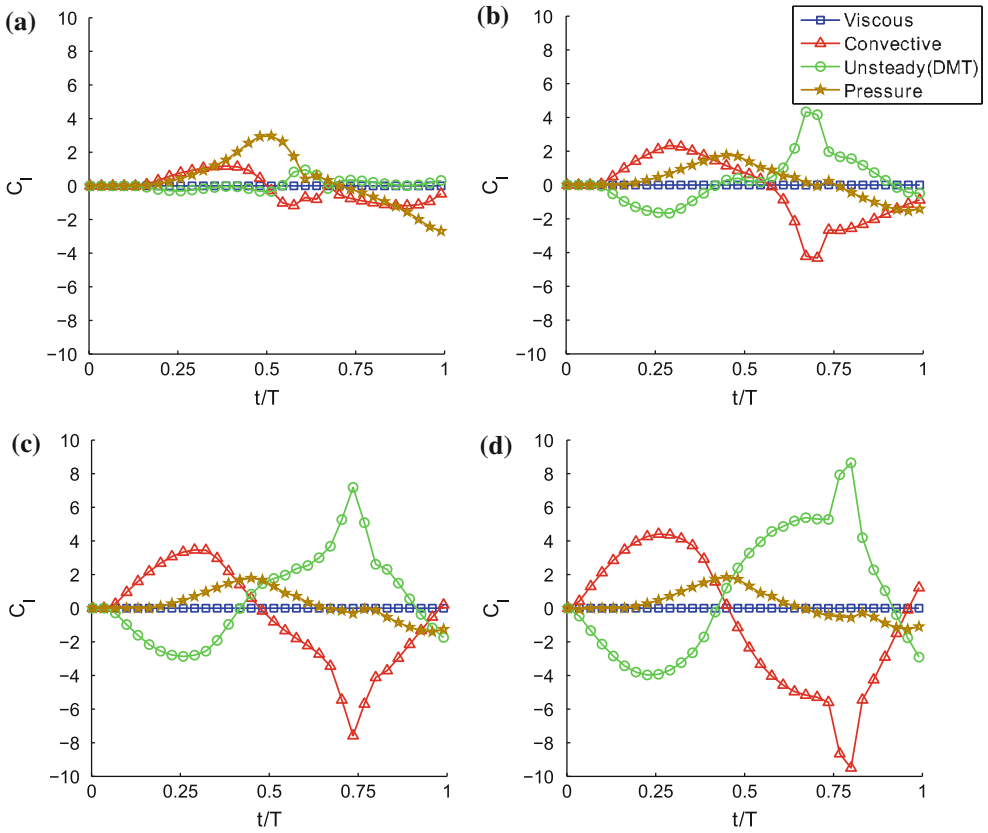

Fig. 4 Contribution of viscous, convective, unsteady and pressure terms for various CVs in the direction of lift; note that the curves have been plotted at every tenth time step for sake of clarity. **a** CV_1. **b** CV_2. **c** CV_3. **d** CV_4

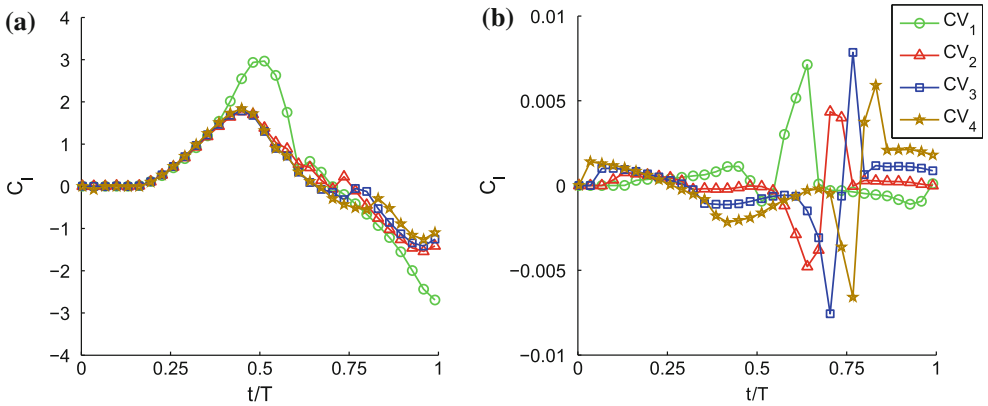

Fig. 5 Assessment of the pressure and the viscous terms toward lift for various CVs. **a** Pressure contribution. **b** Viscous contribution

Figure 6a–d elucidates the contributions of all terms in the direction of drag for CV_1 through CV_4. It can be seen that with the exception of the viscous term, all other terms have approximately the same level of importance. It should be noted that the fluctuation in the pressure term is considerable in this direction. This strong variation in the pressure term is due to the wake vortices, which causes significant changes in the pressure and the velocity profiles.

Figure 7 shows the drag contributions of the pressure and viscous terms over a gust period for CV_1 through CV_4. As shown in Fig. 5a, the pressure term has approximately the same level of importance for all the control volumes. In addition, the peaks represent the time when wake vortices pass across the rear control surfaces. Moreover, at these particular time steps, corresponding peaks of acceleration in Figs. 4 and 6 are observed. Figure 5b illustrates the contribution of the viscous term over time for all control

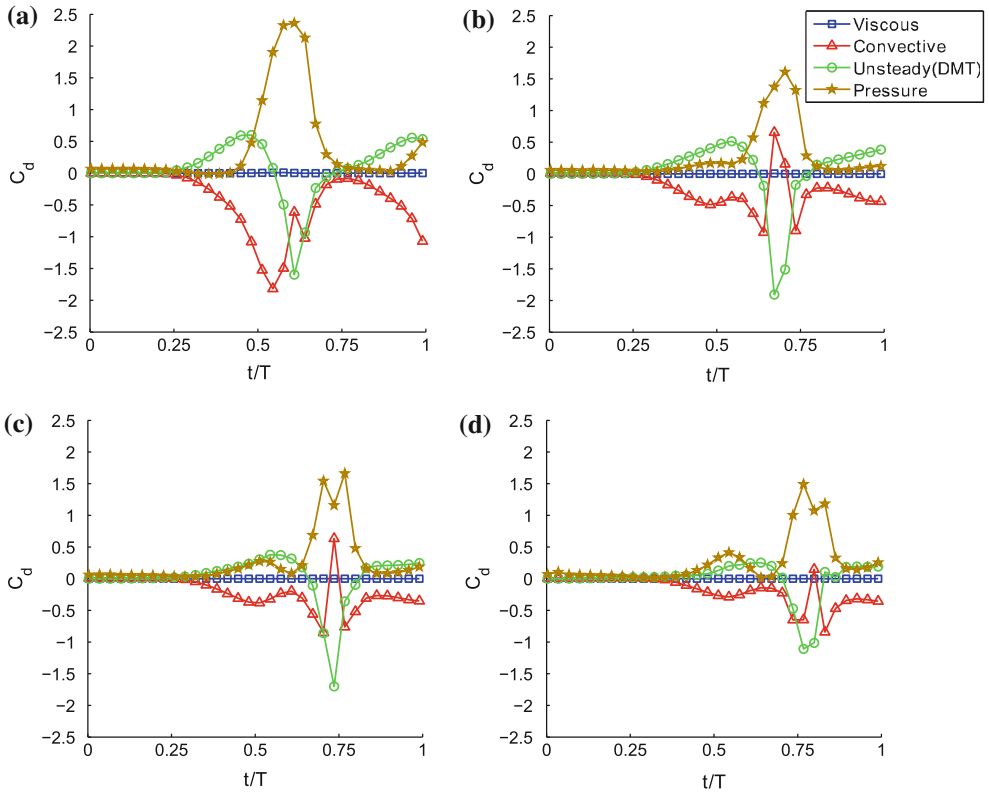

Fig. 6 Contribution of viscous, convective, unsteady and pressure terms for various CVs in the direction of drag; note that the curves have been plotted at every tenth time step for sake of clarity. **a** CV_1. **b** CV_2. **c** CV_3. **d** CV_4

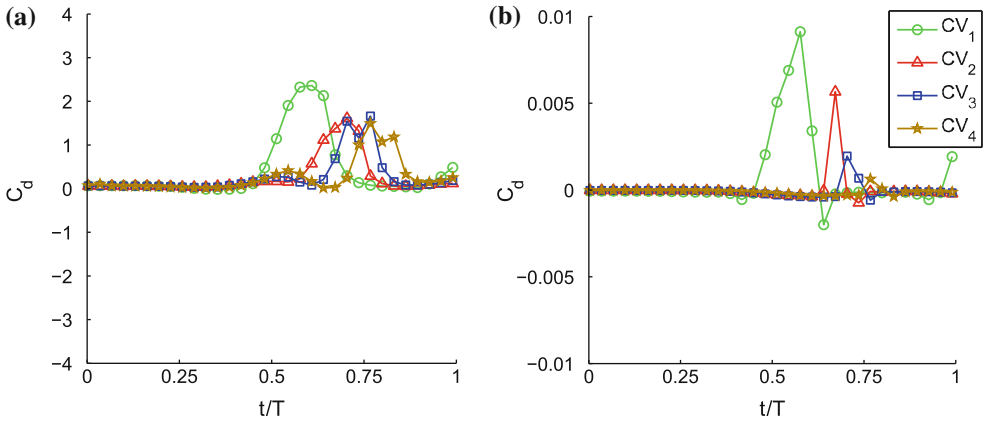

Fig. 7 Assessment of the pressure and the viscous terms toward drag for various CVs. **a** Pressure contribution. **b** Viscous contribution

volumes. It can be seen that the contribution of this term diminishes with increasing control-volume size. This term has less than a 2 % contribution to the total value of drag for the smallest control volume in this study.

4.3 Overall aerodynamic force

In this section, the overall unsteady force is computed using a number of methods. The results that have been obtained by the DMT method are compared with the direct force from pressure and wall shear stress integrations as well as from a classical CV method. In addition, the results for the quasi-steady case, neglecting the unsteady term, are also compared with the direct, classical and DMT methods. Figure 8a–d shows the lift coefficient versus non-dimensional time for CV_1 through CV_4 in the direction of lift. It can be seen that direct, classical and DMT methods are in good agreement with each other. The maximum deviation in C_l computed by the DMT method compared to the direct force values for all CVs is less than 10 %. Moreover, the

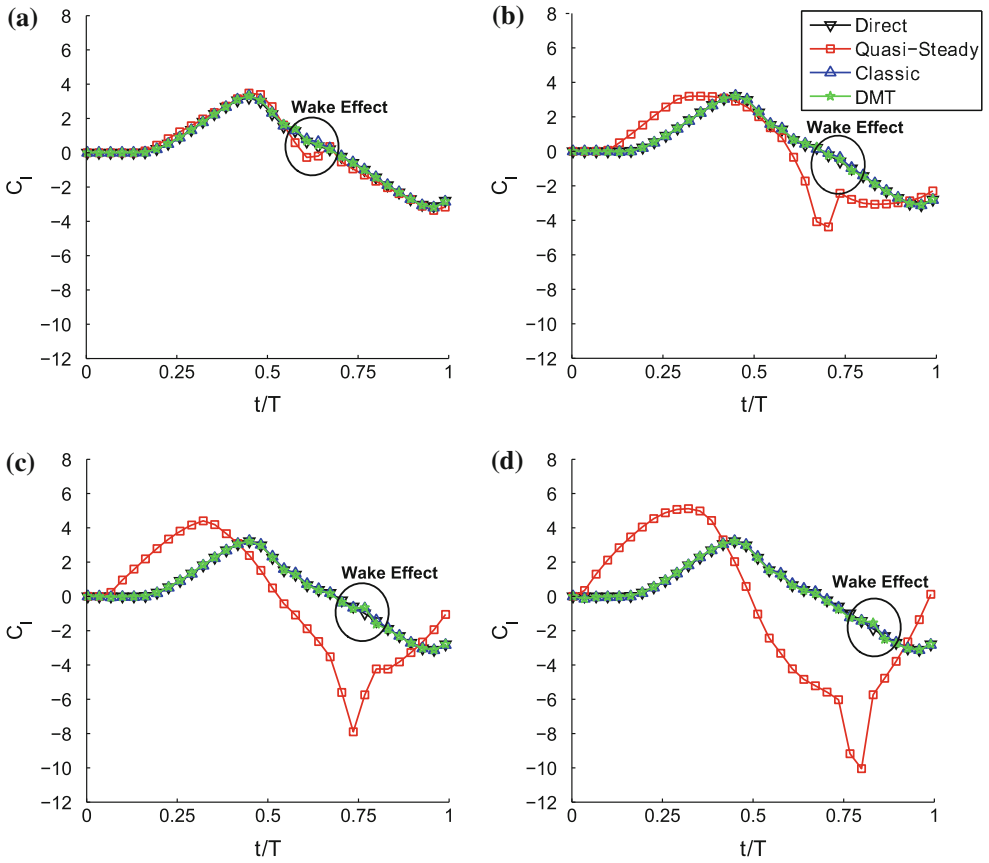

Fig. 8 Lift coefficient computed with four different methods; note that for the quasi-steady curve the unsteady term has been neglected. Also note that all the curves have been plotted at every tenth time step for sake of clarity. **a** CV_1. **b** CV_2. **c** CV_3. **d** CV_4

quasi-steady curve has reasonable agreement for CV_1, while it varies drastically for the larger CVs. The relative behavior of the unsteady term can be shown in Fig. 4a–d. In Fig. 4a, the unsteady term is almost negligible in comparison with the other terms except for the interval of $0.55 \leq t/T \leq 0.65$. This is the particular interval where the quasi-steady curve deviates drastically from the direct-method curve in Fig. 8a. Note that the leading-edge vortex begins to shed and leaves CV_1 in this interval. On the other hand, in Fig. 8b–d, due do the effective contribution of the unsteady term, the quasi-steady curves are in poor agreement with the direct-method curve. As a result, the quasi-steady curve can be used as a rough estimation of lift only for small CVs such as CV_1. Also noteworthy in Fig. 8a–d is the fact that varying CV size maintains an excellent prediction of the overall aerodynamic lift. In Fig. 8, the intervals where the wake vortices pass through the control surfaces have been marked by a circle titled *wake effect*. In these small intervals, the DMT method deviates from the direct-method curve only slightly; the maximum deviation in lift computed by these two methods is approximately 10 %. Note that the pressure and velocity gradients are extremely high over these intervals. Therefore, the pressure integration as well as the calculation of the time derivatives are subjected to error propagation, which leads to deviation of the DMT method from the direct-method curve.

Figure 9 displays the overall drag coefficient computed with four different methods for CV_1–CV_4. Based on Fig. 6, the unsteady term is significant for all CVs in the direction of drag. Therefore, it comes as no surprise that the quasi-steady curve deviates drastically from the other curves. In Fig. 9a–d, the DMT and classical methods are found to be in good agreement with the direct-method curve except for the intervals where the wake vortices pass across the control surfaces. It can be seen that at these particular time steps, there is a significant difference between the DMT and the direct methods. Note that predictions here are in poorer agreement than those for lift since the higher gradients of velocity pass through the control surface. Therefore, the effect of error propagation is higher in this direction. As a result, the computation of the drag coefficient is still limited for this configuration, as also discussed by Jardin et al. (2009). A further discussion regarding error propagation is described in the following section.

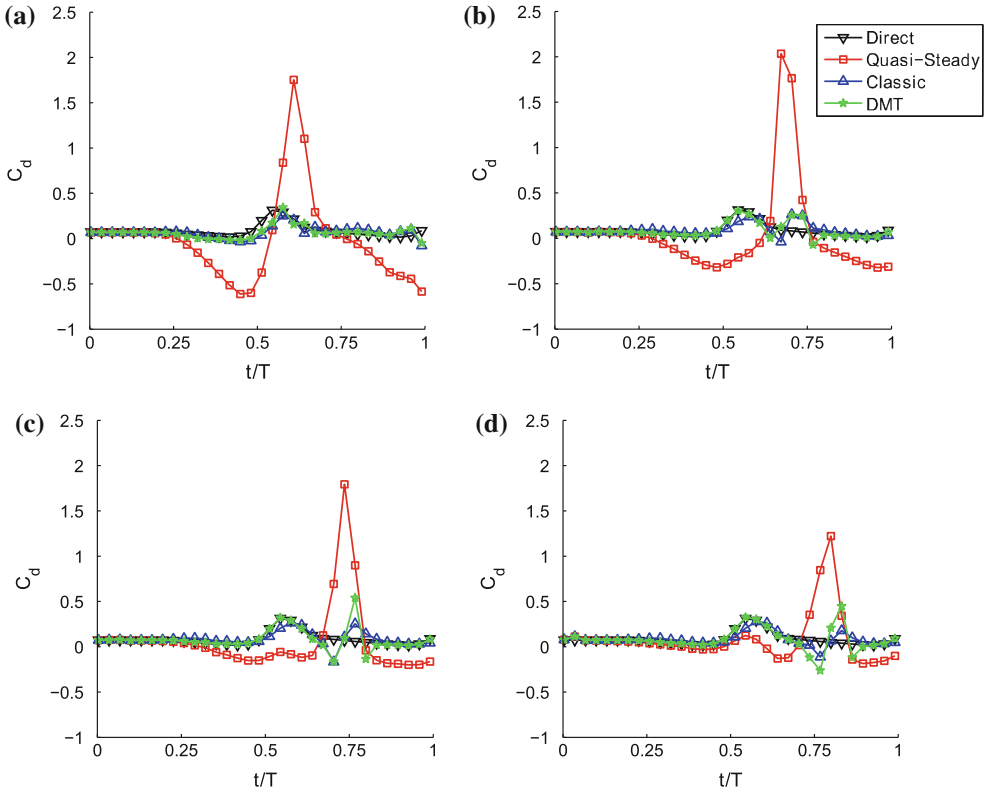

Fig. 9 Drag coefficient computed with four different methods; note that for the quasi-steady curve, the unsteady term has been neglected. Also note that all the curves have been plotted at every tenth time step for sake of clarity. **a** CV_1. **b** CV_2. **c** CV_3. **d** CV_4

4.4 Effect of the vortical wake on the accuracy of the results

As discussed above, the agreement between the DMT and the direct methods is hampered by the wake vortices. The cause for this discrepancy can be attributed to the significant error propagation across the wake as discussed by Kurtulus et al. (2006). The results obtained here show that this detrimental effect is stronger in the direction of drag due to the higher gradients of velocity across the rear surface, leading to significant numerical errors. Figure 10 shows non-dimensional pressure versus non-dimensional time for a period of the gust cycle. In this figure, the pressure distribution along the eastern edges of CV_1 at $t/T = 0.62$ and CV_4 at $t/T = 0.8$ have been shown. Note that at the selected time steps, the wake vortices are close to the eastern edge of the aforementioned control volumes. It should be mentioned that in order to find the absolute pressure distribution along the control volume, the initial value from the CFD solver was taken. It can be seen that the smaller control volume (CV_1) is affected by the strong variation of velocity and pressure on the eastern edge. For smaller control volumes, the high-gradient region affects a large portion of this edge, thus causing a significant numerical error during the integration process. Figure 10d demonstrates good agreement between the values of the pressure term calculated by the direct and DMT methods for the eastern edge belonging to CV_4. The maximum absolute deviation for CV_1 and CV_4 is 0.12 and 0.04, respectively. Furthermore, the evaluation of the unsteady term is also affected by the wake vortices, especially in the direction of drag, due to the time derivatives of the velocity field as shown in Fig. 3b. Therefore, in order to obtain accurate results when the wake vortices pass across control surfaces, very fine temporal and spacial resolutions are required.

In conclusion, the pressure-term evaluation is subject to error propagation due to the spatial integration of the pressure gradient along each control surface. The numerical errors increase significantly when the wake vortices are close to the control surfaces. It should be noted that the results for larger control volumes have the least maximum absolute deviation in the evaluation of the pressure term. Moreover, the classical and DMT methods fail whenever there is a strong fluctuation in the pressure term because of the passing of the wake vortices over the period. The detrimental effect due to pressure is found to decrease with increasing CV size, therefore larger CVs are less sensitive to this source of error.

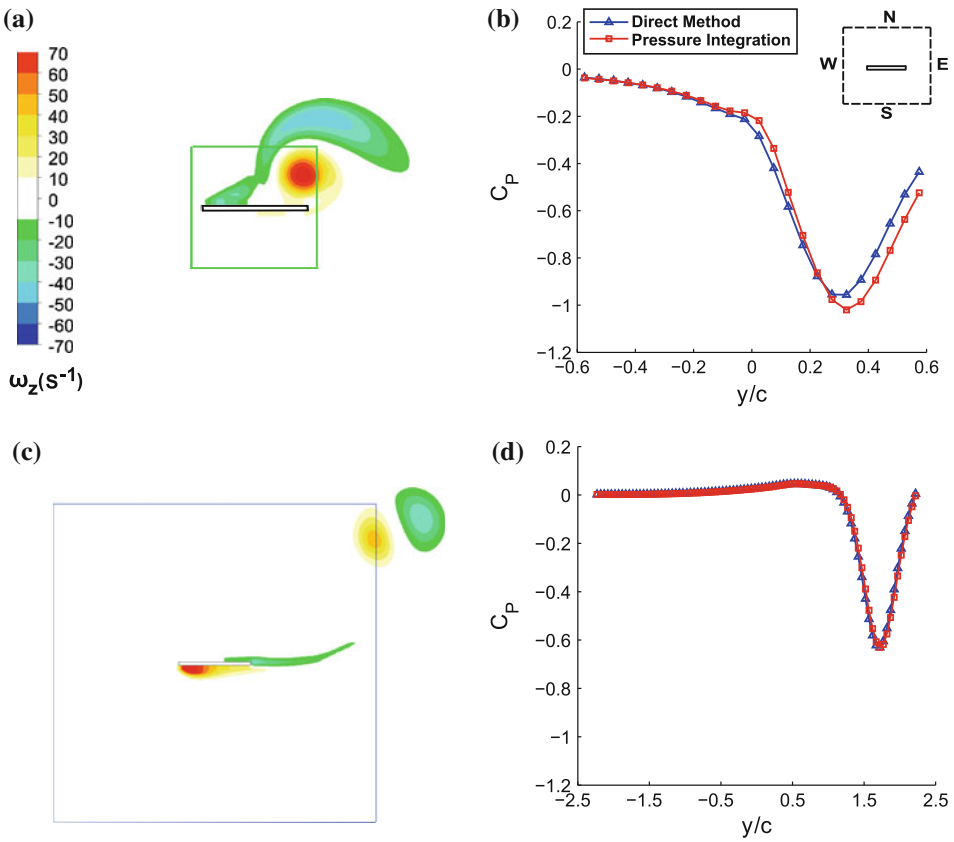

Fig. 10 Pressure distributions along the eastern edges of CV_1 and CV_3 at $t/T = 0.62$ and $t/T = 0.8$, respectively. Note that flow passes from left (western) edge. **a** Vorticity contours across CV_1 at $t/T = 0.62$. **b** Pressure distribution on eastern edge of CV_1 at $t/T = 0.62$. **c** Vorticity contours across CV_4 at $t/T = 0.8$. **d** Pressure distribution on eastern edge of CV_4 at $t/T = 0.8$

4.5 Effect of varying CV size with realistic spatial resolution

In the previous analysis, the distance between two successive vectors for all CVs was held constant. However, to better mimic the realistic camera-chip resolution of a PIV camera, the vector spacing was varied proportional to CV size instead. Figure 11 shows the overall unsteady force in the direction of lift for all CVs. In Fig. 11a, the distance between two successive nodes on each edge of the CV is the same for all cases. For CV_1 through CV_4 the number of nodes is equal to 25, 51, 71 and 91, respectively. In Fig. 11b, the number of nodes on each edge of the CV is held constant and is equal to 25. In Fig. 11a, the maximum absolute deviation in C_l for CV_1 through CV_4 is less than 0.065. In Fig. 11b, the results are far less accurate for the more realistic case; especially for the time intervals when the wake vortices pass through the control surfaces. The maximum absolute deviation in C_l for CV_1 through CV_4 is approximately 1.5. It can be seen that as the spatial resolution is refined, the agreement between the DMT and direct-method curves improves. In addition, it was found that the results in this study agree with Unal et al. (1997) in that accurate results are obtained only for higher spatial resolutions, and therefore, implicitly also higher temporal resolutions.

As a first estimate, it is assumed that only wake vortices greater than or equal to 10 % of the chordlength affect unsteady loadings. Thus, it can be estimated that the control-surface spatial resolution should also be smaller or equal to 10 % of the chordlength in order to capture such vortical structures in the wake. Therefore, the necessary spatial resolution can be estimated as follows:

$$\triangle x = \triangle y \simeq \frac{c}{10}. \tag{17}$$

The CFL condition can be deemed as an acceptable way to estimate a suitable value for the time step. Therefore, for a two-dimensional problem, the time step can be determined as:

$$\triangle t = \min\left(\triangle t = \frac{\triangle x}{\max(u_x)}, \triangle t = \frac{\triangle y}{\max(u_y)}\right), \tag{18}$$

where u_x and u_y are velocity components in the horizontal and vertical directions, respectively. The CV size in this study can be expressed as follows:

$$\alpha c = n\triangle x, \tag{19}$$

where n is equal to the number of nodes and α is the following ratio:

$$\alpha = \frac{CV_{\text{size}}}{c}. \tag{20}$$

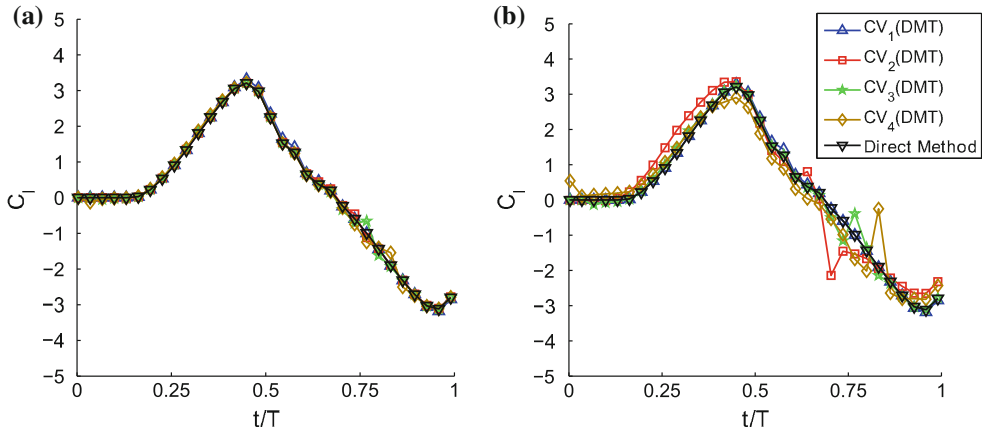

Fig. 11 Effect of varying CV size with scaled and realistic spatial resolutions; note that for the scaled case, the distance between two successive nodes is equal while for the realistic case, the number of nodes on each control surface is constant. All curves have been plotted every tenth time step for sake of clarity. **a** Scaled case with constant vector spacing. **b** Realistic case with varying vector spacing

When comparing to the original estimate of minimum spatial resolution, results from this study (Fig. 11b) suggest that the maximum deviation of the lift coefficient is roughly 10 % when the following relation is satisfied:

$$\frac{\alpha}{n} \leq 0.05, \tag{21}$$

Such that the necessary spatial resolution is closer to 5 % of chordlength. Returning to Eq. (18), this limitation for the time step can now be rewritten such that:

$$\triangle t = \min\left(\triangle t = \frac{\alpha c}{\max(u_x)n}, \triangle t = \frac{\alpha c}{\max(u_y)n}\right). \tag{22}$$

Thus, as a generalization for thin profiles, these above constraints in space and time should be considered when planning future experiments using the DMT method.

5 Conclusions

A comparison of various force-estimation techniques for a two-dimensional flat plate in gusty conditions has been performed using a synthetic data set. The aerodynamic forces have been obtained using a classic control-volume approach as well as with the DMT method and were compared with direct forces obtained from the combined shear-stress and pressure distributions. The DMT method avoids challenges associated with the classical method in the evaluation of the unsteady term through the conversion of the volume integral term into a surface integral. The results demonstrate that the DMT method works well for the evaluation of the unsteady term in both lift and drag directions. In addition, the contribution of various terms in the Navier–Stokes equations is discussed. It was shown that the viscous term is negligible in comparison with the other terms for both lift and drag directions, while the value of the pressure term depends on the position of the control volume relative to the plate. In regions near the body, the value of the pressure term is significant. It can be seen that the convective and unsteady terms are opposite in phase over a period. In the direction of drag, these two terms as well as the pressure term are equal in magnitude, irrespective of CV size. On the other hand, in the direction of lift, the contribution of the pressure term goes to zero when increasing the CV size.

The unsteady term is nearly negligible for CV_1 such that the quasi-steady case can be used as a rough estimation of the overall lift force. It was also shown that at time intervals when the wake vortices pass across the control surfaces, the pressure integration and also the evaluation of the unsteady term introduce large sources of error. This effect is particularly prominent in the direction of drag due to the higher gradients of velocity on the downstream control surface. This effect is also more severe for smaller CVs where the wake vortices cover a larger portion of the downstream control surface.

It was shown that varying CV size does not have a substantial effect on the overall aerodynamic force except for periods where the wake vortices pass through the control surfaces. Therefore, it is suggested that in order to obtain more accurate results, the control volume should be sufficiently far away from the body, which leads to a reduction in error propagation during the evaluation of the pressure and unsteady terms. However, to better represent the realistic camera-chip resolution of a PIV camera, a comparison between the realistic and scaled cases was presented for various CVs. It was shown that for the realistic case and with larger CVs, the coarser spatial resolution dramatically reduces the DMT method's accuracy. Thus, a careful compromise is required in the determination

of the control-volume size when planning future experiments with the DMT method.

Acknowledgments The authors would like to acknowledge the useful suggestions provided by the referees.

References

David L, Jardin T, Farcy A (2009) On the non-intrusive evaluation of fluid forces with the momentum equation approach. Measurement Science and Technology 20 No. 9, 095401 (11pp)

Jardin T, Chatellier L, Farcy A, David L (2009) Correlation between vortex structures and unsteady loads for flapping motion in hover. Exp Fluids 47:655–664

Kat R, Oudheusden BW, Scarano F (2008) Instantaneous planar pressure field determination around a square-section cylinder based on time-resolved stereo-PIV. In: 14th international symposium on applications of laser techniques to fluid mechanics in Lisbon

Kurtulus DF, Scarano F, David L (2006) Unsteady aerodynamics force estimation on a square cylinder by TR-PIV. Exp Fluids 42:185–196

Noca F, Shiels D, Jeon D (1997) Measuring instantaneous fluid dynamic forces on bodies, using only velocity fields and their derivatives. J Fluids Struct 11:345–350

Noca F, Shiels D, Jeon D (1999) A comparison of methods for evaluating time-dependent fluid dynamic forces on bodies, using only velocity fields and their derivatives. J Fluids Struct 13:551–578

Rival D, Manejev R, Tropea C (2010) Measurement of parallel blade-vortex interaction at low Reynolds numbers. Exp Fluids 49:89–99

Rival D, Prangemeier T, Tropea C (2009) The influence of airfoil kinematics on the formation of leading-edge vortices in bio-inspired flight. Exp Fluids 46(5):823–833

Rival D, Schönweitz D, Tropea C (2011) Vortex interaction of tandem pitching and plunging plates: a two-dimensional model of hovering dragonfly-like flight. Bioinspiration Biomimetics 6(1):016008

Unal M, Lin J-C, Rockwell D (1997) Force prediction by PIV imaging: a momentum-based approach. J Fluids Struct 11:965–971

van Oudheusden BW, Scarano F, Roosenboom EWM, Casimiri EWF, Souverein LJ (2007) Evaluation of integral forces and pressure fields from planar velocimetry data for incompressible and compressible flows. Exp Fluids 43(2–3):153–162

Wu J-Z, Pan Z-L, Lu X-Y (2005) Unsteady fluid-dynamic force solely in terms of control-surface integral. Phys Fluids 17:098102-1